Implementation and Validation of the Spalart-Allmaras Curvature Correction in PHASTA

1 INTRODUCTION

It is well-known that the presence of rotation and streamline curvature (RC) substantially alters the physics of turbulent shear flows. Bradshaw [1] notes that these changes are "surprisingly large," in that they are usually "an order of magnitude more important than normal pressure gradients and other explicit terms" in the RANS equations for curved flows. This can lead to significant effects on shear stresses and other quantities when the stream-wise radius of curvature is as large as one hundred times the shear layer thickness [1]. For aerodynamicists in particular, RC phenomena have high impact on boundary layer development, turbulent mixing, and heat transfer in applications ranging from flow over high-camber airfoils to rapidly-rotating turbomachinery blades.

For computational studies to effectively guide developments in design areas dominated by RC-effects, it is imperative that the turbulence models employed capture their influence in some way. Reynolds stress transport (RST) models are sometimes viewed as superior to simpler eddy-viscosity models, because RC terms appear explicitly in the Reynolds transport equation. However, this explicit influence is limited to the production term, and there appears to be little consensus on how rotation and curvature influence the other diffusion and destruction terms [7]. Despite the philosophical advantages that may exist, the accuracy of full RST models comes at substantial computational cost. Accordingly, adding an RC-correction term to the latter class of models would be a boon for workflows that require rapid design iteration.

The Spalart-Allmaras (SA) one equation turbulence model captures important features of aerodynamic flows involving complex geometry and adverse pressure gradients well, and is thus one of the most appropriate eddy-viscosity models for such studies [6]. However, the original model neglects the effects of streamline curvature and rotation. To remedy this, Shur et al. [4] develop an RC-correction term that scales eddy-viscosity production, giving rise to the SARC model. They validate their correction against experimental and DNS data of a number of canonical wall-bounded turbulent shear flows:

- one-dimensional, fully-developed flow in a plane rotating channel,
- one-dimensional, fully-developed flow in a curved channel,
- two-dimensional flow in a channel with a U-turn, and
- three-dimensional flow in a channel of rectangular cross-section with a 90°streamwise bend.

In all cases, the authors demonstrate substantial improvements of the SARC model over the standard SA model and in most cases the Menter two-equation shear stress transport (M-SST). These conclusions are based on predictions of mean velocity and wall shear stress distributions.

In the present project, the Shur et al. [4] curvature-correction (sans rotation terms) is added to the existing SA model in PHASTA, the Parallel Hierarchic Adaptive Stabilized Transient Analysis CFD code developed and maintained by Prof. Kenneth E. Jansen's group at the University of Colorado at Boulder. Our group focuses on aerodynamic flow control, which in many cases simplifies to "the pursuit of bent

streamlines". Of particular interest to the author is the increased accuracy curvature-correction could bring to performance predictions of flow control strategies in an aggressive subsonic diffuser. Other applications include unsteady separation in flows over high-lift wing and tail configurations. Thus, the ability to run curvature-corrected RANS simulations will be a welcome addition to our research capabilities. To test our implementation's correctness, we simulate the $90°$-bend case listed above, verify it using both the SA and SARC data of Shur et al. [4], and validate it against the experimental data of Kim and Patel [3].

With the motivation clear, the remainder of this paper discusses the philosophy underpinning the mathematics of the RC-correction; the changes made to PHASTA during implementation; and the validation procedures employed, including geometry construction, meshing, and comparison to the published data mentioned above.

2   SPALART-ALLMARAS MODEL

As the standard Spalart-Allmaras (SA) one-equation model [6] is our point of departure for the RC-correction, a brief overview is apropos.

The SA model was developed as a middle-ground between algebraic and two-equation models. It sought to address algebraic models' shortcomings in massively-separated flows, while retaining some advantages of two-equation models and forgoing their additional computational complexity. It is tuned specifically for aerodynamic flows, which can exhibit substantial separation and involve complex geometries. Its derivation starts from a blank slate; production, transport, and diffusion terms are constructed from scratch using dimensional and invariance arguments applied to four canonical flows.

Fundamentally, the SA model solves a transport equation for the pseudo-eddy-viscosity $\tilde{\nu}$, which is calibrated to behave properly within the log layer, and then scales it to the canonical eddy-viscosity ν_T in a manner consistent with the viscous sublayer. PHASTA's current version of the SA model omits the original reference's trip term[1], and chooses the vorticity magnitude as the scalar norm of the deformation tensor. The model, as implemented, can be written in full detail as

$$\frac{\partial \tilde{\nu}}{\partial t} + u_j \frac{\partial \tilde{\nu}}{\partial x_j} = c_{b1}\tilde{\Omega}\tilde{\nu} - c_{w1}f_w\left(\frac{\tilde{\nu}}{d}\right)^2 + \frac{1}{\sigma}\left[\frac{\partial}{\partial x_j}\left((\nu + \tilde{\nu})\frac{\partial \tilde{\nu}}{\partial x_j}\right) + c_{b2}\frac{\partial \tilde{\nu}}{\partial x_j}\frac{\partial \tilde{\nu}}{\partial x_j}\right]\,, \tag{1}$$

$$
\begin{aligned}
&\nu_T = \tilde{\nu}f_{v1} &&f_{v1} = \frac{\chi^3}{\chi^3 + c_{v1}^3} &&\chi = \frac{\tilde{\nu}}{\nu} \\
&\tilde{\Omega} = \Omega + \frac{\tilde{\nu}}{\kappa^2 d^2}f_{v2} &&f_{v2} = 1 - \frac{\chi}{1 + \chi f_{v1}} &&\Omega = \sqrt{2\omega_{ij}\omega_{ij}} \\
&\omega_{ij} = \frac{1}{2}\left(\frac{\partial u_i}{\partial x_j} - \frac{\partial u_j}{\partial x_i}\right) &&f_w = g\left[\frac{1 + c_{w3}^6}{g^6 + c_{w3}^6}\right]^{1/6} &&g = r + c_{w2}(r^6 - r) \\
& && &&r = \min\left[\frac{\tilde{\nu}}{\tilde{S}\kappa^2 d^2}, 10\right]\,,
\end{aligned}
\tag{2}
$$

$$
\begin{aligned}
&c_{b1} = 0.1355 &&c_{b2} = 0.622 &&\sigma = 2/3 &&\kappa = 0.41 \\
&c_{v1} = 7.1 &&c_{w2} = 0.3 &&c_{w3} = 2 &&c_{w1} = \frac{c_{b1}}{\kappa^2} + \frac{1 + c_{b2}}{\sigma}\,,
\end{aligned}
\tag{3}
$$

where d is the distance to the nearest wall. Because this model has been extensively summarized in prior work for this course, further exposition will be left to Spalart and Allmaras [6], and we instead move on to a discussion of the Spalart-Shur RC-correction.

---

[1]Technically, PHASTA's version of the SA model corresponds to SA-noft2 on the NASA Turbulence Modelling Resource website.

3   SPALART-SHUR CURVATURE-CORRECTION

The key concepts underpinning the RC-correction were proposed by Spalart and Shur [7], and are understandably similar to those used in developing the SA model due to Spalart's hand in both formulations. Our examination of these concepts is paraphrased and condensed in large part from the aforementioned source. As a precursor, we note that assessments of the 'strength' of rotation and curvature are made relative to the shear rate and inverse shear-layer thickness, respectively.

To develop or critique any RC-correction, it is of paramount importance that one understand the mechanisms by which rotation and curvature influence turbulent flows. Spalart and Shur [7] consider two extreme cases for their model: (a) thin shear flows with weak rotation or weak curvature, and (b) homogeneous rotating shear flows, in which strong rotation eliminates the anisotropic Reynolds stresses ($\tau'_{ij} \equiv -\overline{u'_i u'_j} \to 0$ for $i \neq j$). Intuitive reasoning based on the former suggests a non-dimensional measure of RC-effects, which the authors determine is adequate to employ in the latter case.

For analysis, we assume a statistically-stationary two-dimensional shear flow with mean velocity $\overline{u}$ in the x direction and positive $\partial \overline{u}/\partial y$. We seek to understand the behavior of the Reynolds shear stress $-\overline{u'v'} > 0$, in order to clarify its effects on the eddy-viscosity-based SA model. To correct the Reynolds stress transport equation (RSTE) for reference frame rotation, one must add the term

$$2\Omega'_k \left(\overline{u'_j u'_m} \epsilon_{ikm} + \overline{u'_i u'_m} \epsilon_{jkm} \right) \quad \to \quad 2\Omega' \left(\overline{u'^2} - \overline{v'^2} \right), \tag{4}$$

where Ω' is the rotation rate about the z-axis, and the simplification applies to our two-dimensional shear flow. Since the stream-wise fluctuations are greater than their span-wise counterparts, the Coriolis term increases production of shear stress when $\Omega' > 0$, and vice versa. Curvature produces a similar term in the RSTE. We conclude that the means by which Reynolds stresses are enhanced or diminished in RC-present flows are subtle.

To maintain the original SA model's strengths, any indicator of rotation and curvature we devise must be invariant under Galilean transformations. Since $\overline{u'^2} > \overline{v'^2}$ is the defining turbulent characteristic of our shear flow, it is natural to question what it implies of some standard Galilean invariants of fluid dynamics. As Spalart and Shur [7] discuss, this inequality describes a relationship between between the principal axes of the Reynolds stress tensor τ'_{ij} and the strain tensor $S_{ij} = \frac{1}{2}(u_{i,j} + u_{j,i})$. Depending on the system's rotation direction, the stress axes lag or lead the strain axes. Note that in turbulent flows, the Reynolds stress axes respond slowly to changes in turbulent fluctuations, whereas the strain axes respond rapidly. Based on these tensors' disparate rates of change, in situations where τ'_{ij} leads S_{ij}, the rotation tends to align them with each other, plausibly increasing turbulence production. This mechanism is the central basis of the SARC model, which scales turbulent production based on the alignment of these tensors. Such effects are not readily captured by standard eddy-viscosity models, because the Boussinesq hypothesis assumes stress-strain alignment: $\tau'_{ij} \approx 2\nu_T S_{ij} - \frac{2}{3}k\delta_{ij}$.

It remains to devise a quantitative measure of the degree to which turbulent stress and strain are leading or lagging each other. Such an indicator will ideally recognize the common physical basis of curvature and rotation effects. In the two-dimensional case, Spalart and Shur [7] decide to track the direction of the principal axes of the strain tensor. Defining the angle α as the direction of strain tensor principal axes relative to an inertial frame, the total derivative $D\alpha/Dt$ is chosen. Considering $D\alpha/Dt$ physically, it is apparent that it both tracks curvature and rotation effects, and is Galilean invariant. Note that in a two-dimensional rotating homogeneous flow, $D\alpha/Dt = \Omega'$. Our present discussion is predicated upon the existence of principal strain directions. Situations in which S_{ij} is isotropic result in undefined α, and mitigation strategies will be discussed shortly.

In the full three-dimensional case, the principal directions cannot be easily determined from algebraic manipulations, and the rotation angle α becomes a rotation angle vector. To obtain an invariant similar to

$D\alpha/Dt$ while addressing these additional complexities, Spalart and Shur [7] consider the double contraction

$$\frac{DS_{ij}}{Dt}\frac{\delta S_{ij}}{\delta t} \tag{5}$$

to be a prime candidate, where $\delta S_{ij}/\delta t$ is defined as the point-wise rotation of the strain rate tensor at a rate given by the vorticity vector. Symmetry considerations reveal that this expression depends only on the curl of the velocity field, which is consistent with a quantity targeting only rotation and curvature effects. After normalizing the magnitude using D, an average of the strain and vorticity norms, and including system rotation effects in a similar manner to the two-dimensional case, a scalar measure of RC-effects in three dimensions can be written as

$$\tilde{r} = \frac{2\omega_{ik}S_{jk}}{D^4}\left(\frac{DS_{ij}}{Dt} + \Omega'_m(\epsilon_{imn}S_{jn} + \epsilon_{jmn}S_{in})\right). \tag{6}$$

The connection to (5) is clear from the nature of the contraction and the presence of vorticity from $\delta S_{ij}/\delta t$. The second derivatives of velocity present in DS_{ij}/Dt should not be taken lightly, since they add complexity to the computational implementation. Nonetheless, Spalart and Shur [7] find no reasonable approximations to $\tilde{r}$ that can be calculated using only first derivatives.

Increased computational demand aside, $\tilde{r}$ can be used to construct a scaling function applied to the production term of the SA model. In our PHASTA implementation, we assume a stationary reference frame, setting $\Omega'_m = 0$ and allowing Coriolis terms to vanish. The only modification required to the standard SA model is to multiply the production term $c_{b1}\tilde{S}\tilde{\nu}$ in (1) by a rotation function f_{r1}, where

$$f_{r1} = (1 + c_{r1})\frac{2r^*}{1 + r^*}[1 - c_{r3}\arctan(c_{r2}\tilde{r})] - c_{r1} \tag{7}$$

$$r^* = S/\Omega \qquad \tilde{r} = \frac{2\omega_{ik}S_{jk}}{D^4}\left(\frac{DS_{ij}}{Dt}\right) \qquad S_{ij} = \frac{1}{2}\left(\frac{\partial u_i}{\partial x_j} + \frac{\partial u_j}{\partial x_i}\right)$$

$$S^2 = 2S_{ij}S_{ij} \qquad \Omega^2 = 2\omega_{ij}\omega_{ij} \qquad D^2 = (S^2 + \Omega^2)/2 \tag{8}$$

$$c_{r1} = 1.0 \quad c_{r2} = 12 \quad c_{r3} = 1.0 . \tag{9}$$

This rotation function protects against the case of isotropic stresses mentioned above; though $\tilde{r}$ may blow up as the strain tensor vanishes, f_{r1} effectively turns itself off through the r^* terms. Note that for our original example of shear flows with no curvature, $r^* = 1$, $\tilde{r} = 0$, and the constraint that the original SA model be recovered through $f_{r1} \to 1$ is satisfied. The model constants are tuned using joint numerical-experimental data from Dacles-Mariani et al. [2]. Shur et al. [4] note that these constants are still being tuned, and that for a backward-facing step, they found a value of $c_{r3} = 0.6$ instead of 1 to be more appropriate. Nonetheless, the NASA Turbulence Modelling Resource website lists the values given in (9) as reliable, and we use them accordingly in our own implementation.

4 PHASTA IMPLEMENTATION

Since the standard SA model has already been implemented in PHASTA, our only task is to calculate and pre-multiply its production term by f_{r1}. The material derivative of the strain tensor, DS_{ij}/Dt, in (8) makes this process slightly more complicated than initially anticipated, but not overly so. Because this is the author's first major foray into the source of PHASTA, the decision was made to limit modifications to the incompressible code. In this section, we describe the process used to compute f_{r1}.

4.1 FINITE ELEMENT PRELIMINARIES

Because Spalart-Allmaras is a one-equation model, it requires solution of an additional transport equation for the eddy-viscosity ν_T, in addition to the Navier-Stokes equations. The strong form of the eddy-viscosity transport equation specified in the SA model includes source, convection, and diffusion terms. To translate it into the finite element method's framework, the scalar transport equation is pre-multiplied by a weight function and integrated over the domain. Terms with second-order derivatives, such as diffusion, are integrated by parts to reduce the order of spatial derivatives that must be computed. The SA production term,

$$c_{b1}\tilde{\nu}\left(\sqrt{2\omega_{ij}\omega_{ij}} + f_{v2}\frac{\tilde{\nu}}{\kappa^2 d^2}\right),\tag{10}$$

is just a scalar quantity with no encompassing derivatives, so its only contribution to the weak form residual comes from a spatial integral. No integration by parts is needed, so no surface integrals are affected by the source term.

After localizing the weak form equation to elements, it is apparent that the production term is only evaluated at the quadrature points used for numerical integration. Thus, the most straightforward implementation of the Spalart-Shur curvature correction involves computing the f_{r1} production scaling factor only at quadrature points. Accordingly, any nodal quantities that act as arguments to f_{r1} must be interpolated to these quadrature points. This process is standard in finite elements. Given nodal values ϕ_A^e and shape functions $N_A^e(\mathbf{x}^e)$, the interpolated value $\phi(\mathbf{x}^e)$ at local coordinate $\mathbf{x}^e$ can be expressed as the sum

$$\phi(\mathbf{x}^e) = \sum_A N_A^e(\mathbf{x}^e)\,\phi_A^e,\tag{11}$$

where the superscript e indicates quantities localized to an element. Furthermore, the first derivative of that variable with respect to some coordinate x_i can be written in terms of readily-computed shape function derivatives:

$$\frac{\partial \phi(\mathbf{x}^e)}{\partial x_i} = \sum_A \left(\frac{\partial N}{\partial x_i}\right)_A^e (\mathbf{x}^e)\,\phi_A^e.\tag{12}$$

These formulae will be used routinely to compute arguments of f_{r1} at quadrature points.

Because PHASTA uses linear shape functions, computing spatial second-derivatives is non-trivial. This raises the question of how we intend to compute such derivatives of velocity for the curvature-correction's DS_{ij}/Dt strain gradient terms. Their computation is aided by a projection-reconstruction approach, which proceeds as follows, given nodal values of a scalar ϕ:

1. The slope $\partial \phi/\partial x_i$ is computed between neighboring nodes, projecting a derivative field onto the elements.
2. Slopes computed for neighboring elements are averaged together, reconstructing a nodal representation of $\partial \phi/\partial x_i$.

To obtain spatial second-derivatives, (12) can be applied to the reconstructed field. Fortunately, a nodal reconstruction of a scaled S_{ij} is already computed during each flow solve, and can be made accessible to our scalar solve routines.

4.2 CHANGES TO SOURCE CODE

We begin with general book-keeping changes to the code. First, the "RANS-SARC" model is added as an option to input_fform.c, and assigned an identifying iRANS integer of -3. Since all machinery within the existing SA code will also be used in the curvature-corrected model, any if-statement that activates for the standard SA model (identified by an iRANS code of -1), is also changed to activate for the curvature-corrected model. Spalart-Shur constants from (9) are added to turbsa.f.

The main terms involved in f_{r1}, shown in (8), need to be accessible to the main computation of the eddy-viscosity, also known as the turbulence scalar, source term in e3sourceSclr. The following changes to the PHASTA source we discuss facilitate this need.

As mentioned in the previous subsection, we require the nodal reconstruction of S_{ij} in order to compute its spatial derivative. The scaled reconstruction, $2(\nu + \nu_T)S_{ij}$, is called qres, and its global representation is computed in the flow solve's ElmGMR routine. We pass the variable up through SolFlow to itr-drv, and then down through the increasingly-specific scalar solve routines until we reach e3ivarSclr. Here, we compute the gradient of qres (the local version, at least), and divide through by $2(\nu + \nu_T)$ to retrieve the gradient of S_{ij}, which is then passed into e3sourceSclr. The stack of function calls, starting from itr-drv, is:

- SolSclr
- ElmGMRSclr
- AsIGMRSclr
- e3Sclr
- e3ivarSclr
- e3sourceSclr

Figure 1: Experimental geometry of Kim and Patel [3].

With this minor change, all additional quantities needed have been passed to e3sourceSclr. We now consider subsequent terms used in f_{r1}. The material derivative of the strain rate tensor can be written as

$$\frac{DS_{ij}}{Dt} \equiv \left(\frac{\partial}{\partial t} + u_k \frac{\partial}{\partial x_k}\right) S_{ij} = \frac{\partial}{\partial t}\left[\frac{1}{2}\left(\frac{\partial u_i}{\partial x_j} + \frac{\partial u_j}{\partial x_i}\right)\right] + u_k \frac{\partial S_{ij}}{\partial x_k}$$
$$= \frac{1}{2}\left(\frac{\partial}{\partial x_j}\frac{\partial u_i}{\partial t} + \frac{\partial}{\partial x_i}\frac{\partial u_j}{\partial t}\right) + u_k \frac{\partial S_{ij}}{\partial x_k} = \frac{1}{2}\left(\frac{\partial a_i}{\partial x_j} + \frac{\partial a_j}{\partial x_i}\right) + u_k \frac{\partial S_{ij}}{\partial x_k} , \tag{13}$$

where the fluid acceleration vector is defined as $a_i \equiv \partial u_i/\partial t$, and we have interchanged the order of derivatives by assuming that u_i varies continuously in space and time. Like S_{ij}, a_i is computed during each flow solve. It is already accessible within e3sourceSclr. We need only calculate two spatial derivative tensors, $a_{i,j}$ and $S_{ij,k}$, contracting the latter with velocity u_k, to get DS_{ij}/Dt. Such spatial derivatives are computed in the standard manner of (12). We compute Ω^2, S^2, and D^2 directly in e3sourceSclr using $u_{i,j}$, which already exists in the code for the standard SA model. Computation of f_{r1} is trivial at this point, and proceeds according to (7). Changes to the source can be consulted for specific details of implementation.

5 MODEL VALIDATION

Though the changes to PHASTA are relatively straight-forward, they must be validated against existing experimental (and in this case, computational) data. Without validation, application to novel flows would be circumspect.

5.1 PUBLISHED DATA AND APPROACH

We validate our implementation against both the experimental data of Kim and Patel [3] and the computational data of Shur et al. [4], both of which concern flow through a 90°-bend duct of rectangular cross-section. No system rotation is present.

Kim's experimental geometry is shown in Figure 1. Referencing the top view diagram, flow enters the domain after a contraction section of area ratio 6, and is tripped by sandpaper along all four walls of the duct to generate a fully turbulent boundary layer by the time the flow reaches the bend. The duct has characteristic dimension $H = 8$ in (0.2032 m), with inner and outer radii of $R_i = 3H$ and $R_o = 4H$, respectively. Kim and Patel [3] took special care to isolate secondary flows and vortex formation in the corners from purely curvature-driven effects present along the center-line, and accordingly chose a duct aspect ratio of 6. Thus, the span-wise dimension is H, and the vertical dimension is $6H$.

Kim and Patel [3] report a freestream velocity of $U_0 = 16$ m/s, and a duct Reynolds number of $Re = U_0 H/\nu = 224,000$. This determines the kinematic viscosity to be $\nu = 1.45 \times 10^{-5}$ m^2/s. We assume a typical density of air, $\rho = 1.225$ kg/m^3.

When presenting our validation data, we use the X, Y, Z coordinate system of Kim and Patel [3], which locates the origin at the upper inside corner of the duct exactly where it begins to curve. X is the stream-wise coordinate, Y is the span-wise coordinate perpendicular to X, and Z is the distance from the top duct wall.

Experimental data is collected at seven measurement stations: U1, U2, 15, 45, 75, D1, and D2, listed in the order they are encountered by a fluid particle in the core of the flow. Stations upstream of the bend are denoted 'U', and downstream stations, 'D.' In the curved section itself, the angle between the curved-duct centerline and the straight-inflow duct centerline varies from 0° to 90°. Stations numbered 15, 45, and 75 correspond to those locations. At each station, two measurements are conducted. First, mean streamwise velocity profiles are taken across the Y-direction of the duct at $Z/H = \{1, 2, 3\}$. Second, skin friction values are obtained around half the circumference of the duct cross-section. That is, for a station's fixed X-coordinate, C_f is measured at a range of points starting at the center of the inside (convex) wall ($Z/H = 3$), travelling up to $Z/H = 0$, across the top wall from $Y/H = 0$ to $Y/H = 1$, and then back down the outside (concave) wall to the centerline. Combining the $Z/H = 3$ measurements also exposes the centerline behavior of C_f. These locations can be mapped with a single coordinate $L \in [0, 7]$, which denotes the distance around the circumference described above from the starting point. The locations where C_f data may be plotted for maximum informative impact are summarized in Figure 2.

In developing the SARC model, Shur et al. [4] validate both their SA and SARC results using this same experiment, and we compare to their results for skin friction coefficient C_f. To determine their inlet boundary conditions, the authors ran a straight channel simulation until an adequate turbulent boundary layer developed. These flow and scalar fields were then applied as inflow conditions to their computational
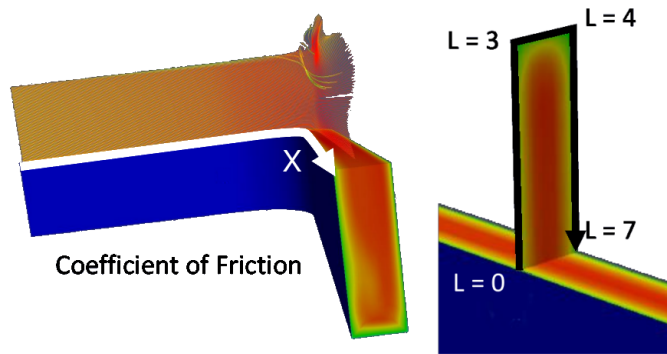
Figure 2: Coordinate systems used for plotting validation data. Left: streamwise coordinate X at duct centerline on inside wall. Right: L describing circumferential distance from inner duct centerline at fixed X.

domain, which starts at station U1. They used a structured $121 \times 81 \times 61$ grid, resulting in $\sim 600{,}000$ hexahedral elements. Mesh anisotropy in the straight sections of the duct, which grades to nearly isotropic elements in the curved section, reduces resource requirements of the simulation.

5.2 VALIDATION PROCEDURE

Three main steps comprised our model validation: mesh generation, inflow condition tuning, and analysis of model behavior. There was some interplay between all three. Renderings of the meshes to be discussed are presented in Figure 5 and Figure 3. All meshes we create are unstructured.

On all meshes we ran, the boundary conditions applied to the computational domain were, unless otherwise noted:

- **Walls:** no slip, zero scalar (ν_T) magnitude
- **Outflow:** zero scalar flux
- **Inflow:** velocity 13.9 m/s (to grow to the experimental freestream velocity of $U_0 = 16$ m/s at U1's centerline; our inflow velocity was changed to 16 m/s by the end of the process), and a free-stream turbulence value of $\nu_T = 4.35 \times 10^{-5}$, which is 3× the kinematic viscosity, in keeping with Spalart [5]

Figure 3: Boundary layer mesh comparison of inflow boundary for meshes A, B, and C (top to bottom).
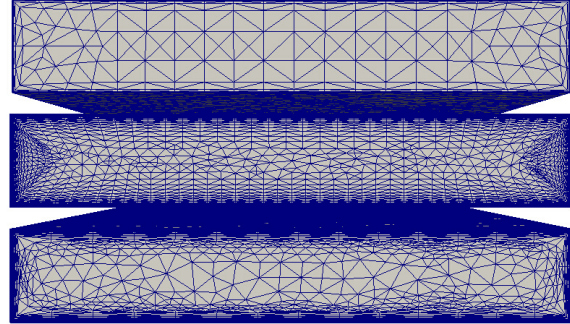
Our first task was to match the experimental velocity profile at station U1. An initial coarse mesh (Mesh A) was generated for this purpose. It was characterized by an inflow (outflow) straight-section length that far exceeded (matched) the experiment's length of 1.52 m (5.18 m). The upstream section was 7.82 m long to facilitate examination of boundary layer (BL) development. An absolute mesh size of 0.2 m $\sim H$ was applied, followed by two refinement boxes with absolute mesh sizes of 0.1 m and 0.05 m, visible in Figure 5. Boundary layers on all physical walls were added and parametrized by: a first layer height of $\Delta y_1 = 2 \times 10^{-6}$, a total thickness of approximately 1/3 the duct height $\Sigma \Delta y = 0.07$, and 10 total out-of-plane layers. Initial BL development studies determined that the $\Delta y_1^+ \sim 5$ recommendation for coarse or exploratory meshes of Spalart [5] was satisfied, as seen in Figure 4. However, the BL mesh's growth rate was too high to provide adequate out-of-plane resolution for comparison with experimental velocity profile at station U1. This inadequacy of Mesh A is shown in the upper item of Figure 3.
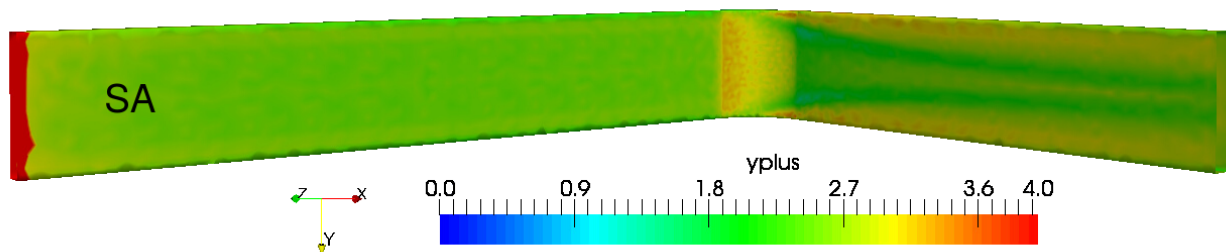
Figure 4: Un-modified SA model run on Mesh A, with y^+ values of the first off-wall mesh points plotted. Maximum value in the curved section is $y^+ \sim 3$. Outer wall has a similar maximum.
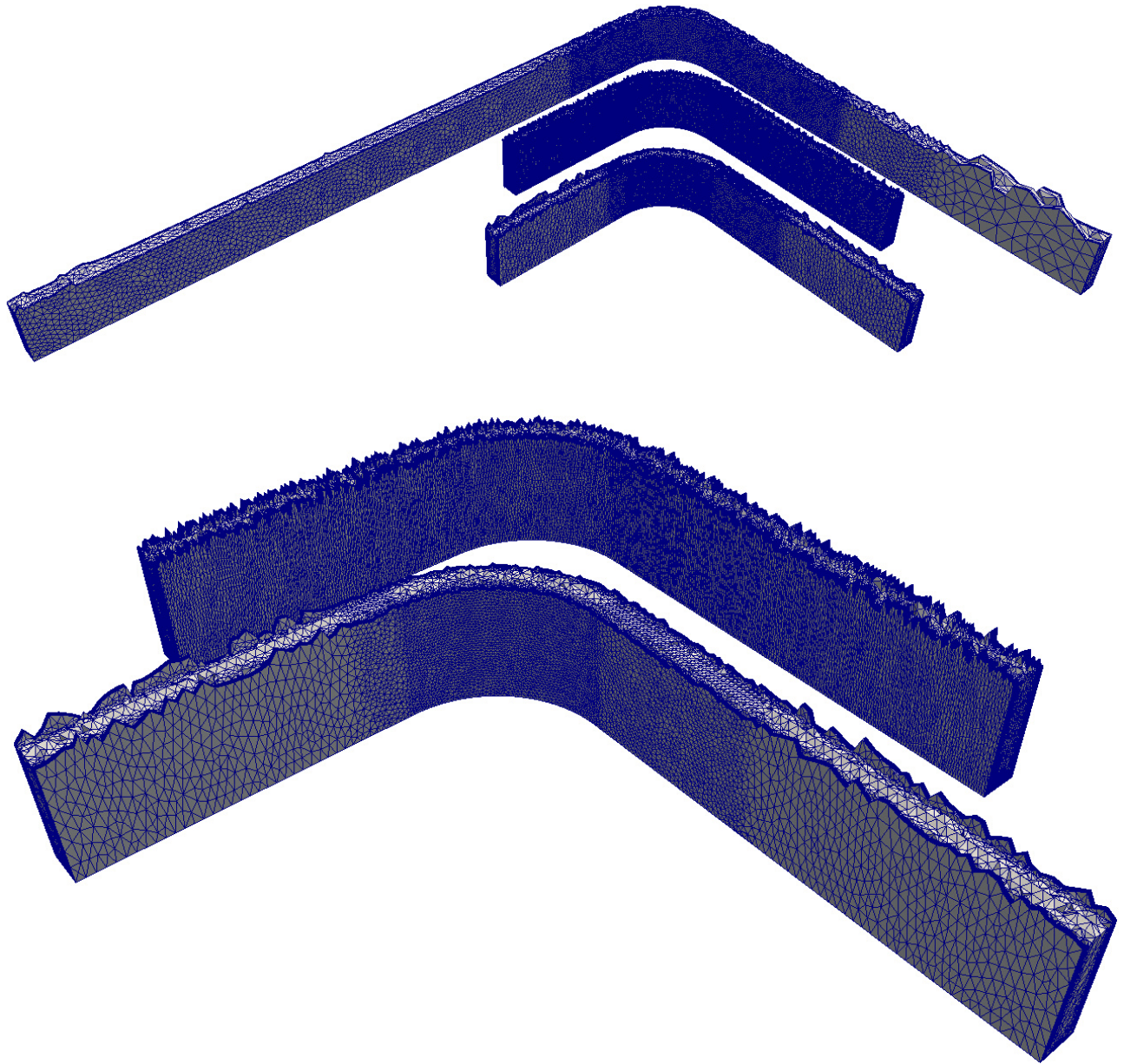
Figure 5: Comparison showing the lower half of meshes cut at $Z/H = 3$. Upper group of three: meshes A, B, and C (top to bottom). Lower group of two: magnified view of meshes B and C (top to bottom). For all meshes, fluid enters from the left.

New meshes were made with lower growth rates, primarily by Riccardo Balin. These meshes allowed for detailed comparisons to be made with experimental velocity profiles at U1. Three major conclusions were drawn from this process. First, velocity BL scaling at the inflow had little affect on matching U1 velocity profiles. Second, adding an eddy viscosity profile in the BL helped achieve good agreement with U1 velocities. This scalar profile plays a similar role to the sandpaper trip in the experimental duct, and develops a steeper BL mean velocity gradient. Third and accordingly, the inflow section of the duct could be substantially shortened (see Meshes B and C in Figure 5) because of expedited turbulent BL development. For these later meshes, the value of Δy_1^+ was iterated upon to meet the recommended value of ~ 2 from Spalart [5]. Mesh B and Mesh C had upstream sections of length 1.69 m, and downstream sections of length 2.5 m. Both had much finer resolution in the Y-direction. Mesh B utilized anisotropic elements, but still resulted in 5.25 million tetrahedra, which was too costly for the negligible improvement it showed over our "final mesh," Mesh C. Mesh C was generated with the following properties, and can again be inspected in Figure 5:

- Anisotropic mesh size of 0.045 m in the X- and Y- directions, 0.09 m in the Z-direction.
- Refinement box of element edge size 0.03 m
- Relative curvature refinement with a value of 0.004
- Boundary layers with $\Delta y_1 = 2 \times 10^{-5}$, $\Sigma \Delta y = 0.027$, and 26 total layers.

Runs on Mesh C are conducted with a time step of 1×10^{-2} sec. It takes about 100 time steps to run through the transient. Though transient results may be interesting for debugging purposes, since we are using first-order time integration and such a large time step, they have little physical import.

5.3 RESULTS AND DISCUSSION

Using Mesh C, we now present results comparing our implementation of the Spalart-Shur curvature correction to those produced by the original SA model.

First and foremost, it is desirable to show evidence that our inflow profile was tuned appropriately to match velocity profiles at U1, and subsequently predict velocity profiles at U2, before effects of curvature come into play. Such profiles are found in Figure 6, and show rather good agreement at all stations and for both models. Exceptions include the outer wall at station 75, where an adverse pressure gradient feeds turbulent mixing and draws high-momentum fluid toward the boundary; and the inside wall at D1, where flow separation occurs due to an adverse pressure gradient at the end of the convex curvature. Pressure in the $Z/H = 3$ plane is shown in Figure 8 to facilitate visualizing the physics. The adequacy of inflow conditions observed here is consistent with later plots of C_f on the walls of the upstream section.

Eddy viscosity behavior is presented in Figure 7 and Figure 8. Published studies on two-dimensional boundary layers indicate that convex curvature has a stabilizing effect on turbulence (i.e. reduces turbulent transport), whereas concave curvature has the opposite effect [3]. Thus, we would expect eddy viscosity to be reduced near the inside wall, while increasing (not necessarily in equal-and-opposite fashion, though) on the outside wall. From Figure 8 we see this behavior in the SA model results, but not quite for SARC. This is our first warning that the curvature-correction may not be correctly implemented. Though the SARC eddy viscosity increases on the outer wall up until about halfway through the bend, it is rapidly and unexpectedly diminished around station 45. On the inner wall, eddy viscosity appears to stay constant. More quantitative comparison between models in Figure 7 confirms these trends.

This odd behavior of the SARC implementation causes strange effects on the wall shear stress shown in Figure 9. Though both models show the expected sharp increase in wall shear stress as flow responds to the favorable pressure gradient on the inside wall, the SA model reflects the trend until curvature disappears. Dissimilarly, mid-way through the curved region, SARC predicts a marked drop in wall shear stress, even in the centerline region (not affected by stream-wise corner vortices that develop at the onset of curvature),
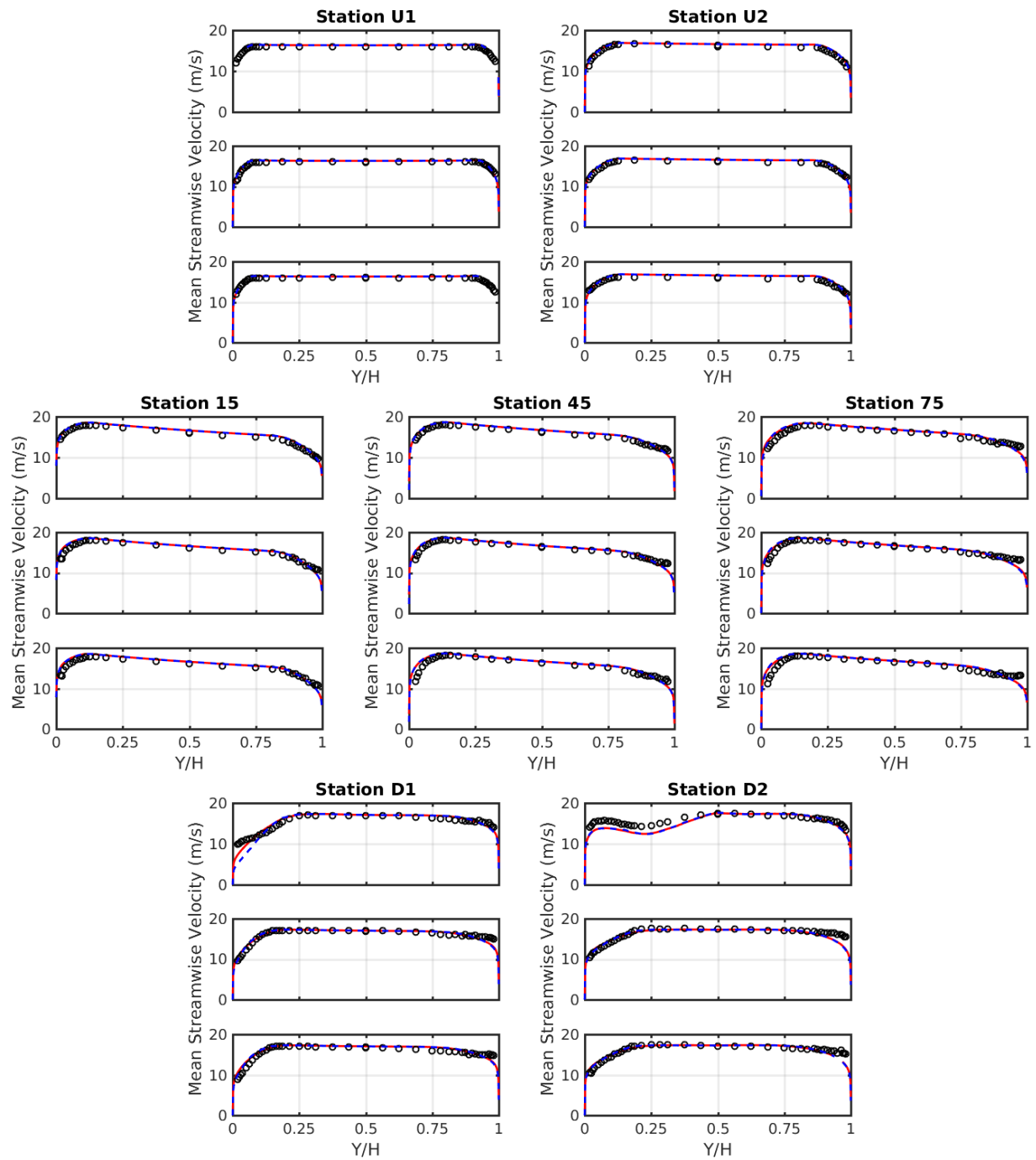
Figure 6: Velocity profiles from Kim and Patel [3] (○), and the SA (——) and SARC (- - -) models at all seven experimental stations. For each station, velocity profiles are shown at $Z/H = 1, 2, 3$, from top to bottom.
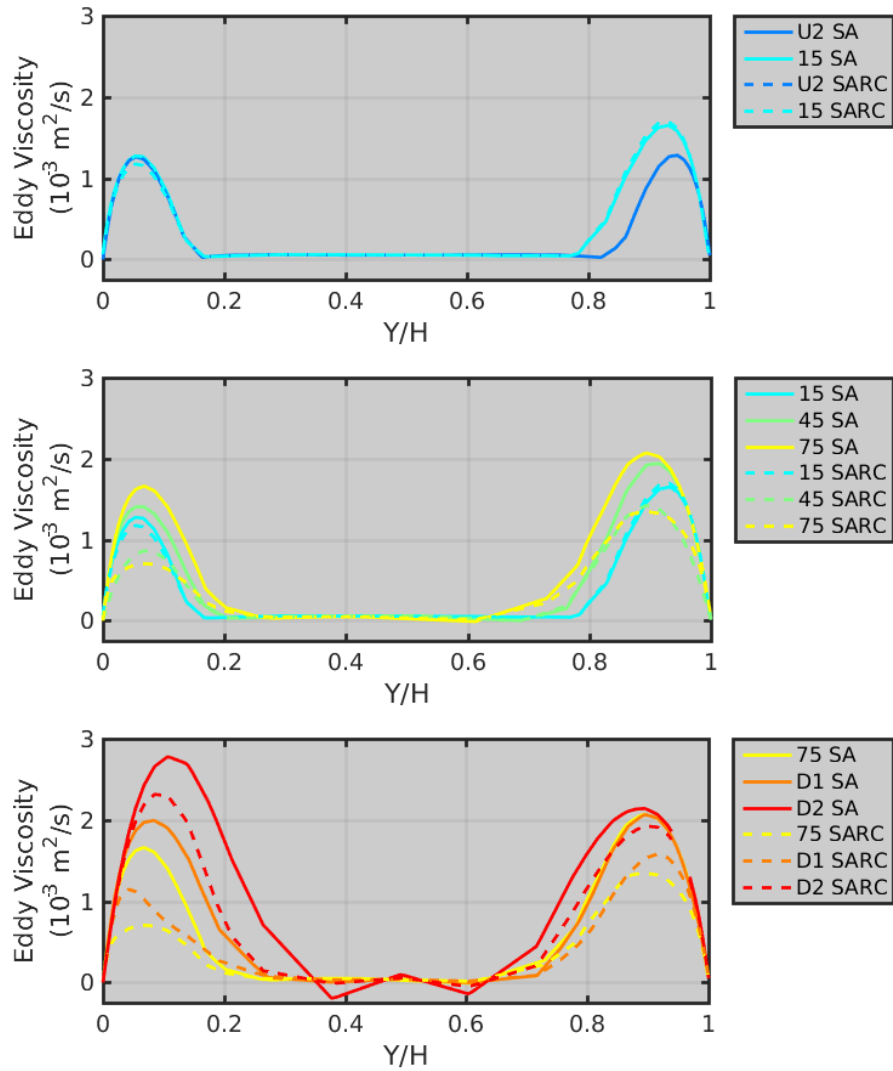
Figure 7: Eddy viscosity behavior comparison between SA (——) and SARC (– – –) at $Z/H = 3$.
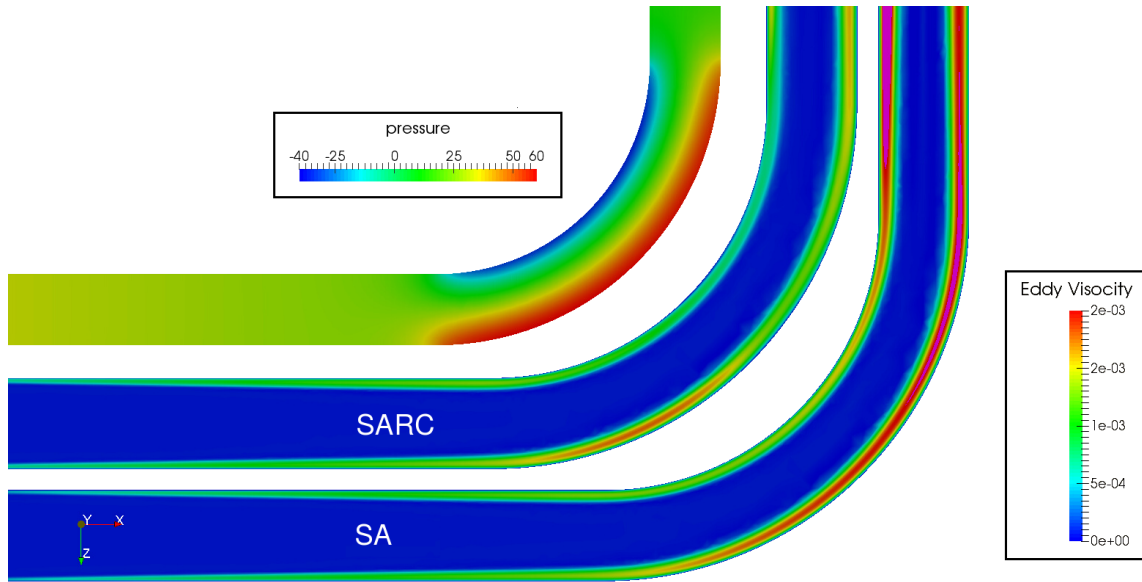
Figure 8: Eddy viscosity (m^2/s) behavior comparison between SA and SARC along a centerline slice ($Z/H = 3$). Pressure (Pascals) is shown concurrently to understand the de/stabilizing effects of pressure gradient on turbulence in the presence of convex/concave walls.
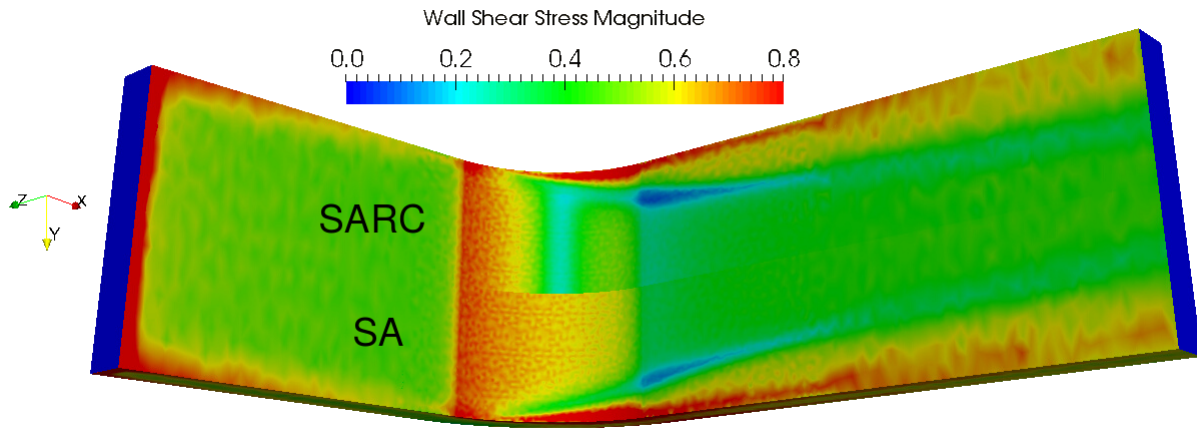

Figure 9: Predicted wall shear stress by SA (bottom) and SARC (top) models.

and despite the fact that the pressure profile remains essentially unchanged for the extent of the curved section (this is true for both SA and SARC results).

This does not bode well for our predictions of friction coefficient, since it is just a scaled version of wall shear stress. This is borne out for C_f along the centerline, Figure 11, and along the circumference of each experimental station, Figure 10. Poor performance of both models away from the $Z/H = 3$ centerline, corresponding to roughly $2 \leq L \leq 5$, is expected, since Mesh C simply does not have the requisite corner resolution to capture the secondary flows and vortical structures accurately. On both walls, the SA model seems to do an excellent job of replicating the SA results of Shur et al. [4], which are shown in Figure 12.

Though a grid-independence study could be formally conducted, I hesitate to do so for two reasons: first, the implementation is still being debugged, and the current mesh has the ability to capture the aberrant behavior pretty clearly; second, the SA results are nearly identical to those on the 5.25 million-element Mesh B (not shown), and also compare favorably with the results of Shur et al. [4].
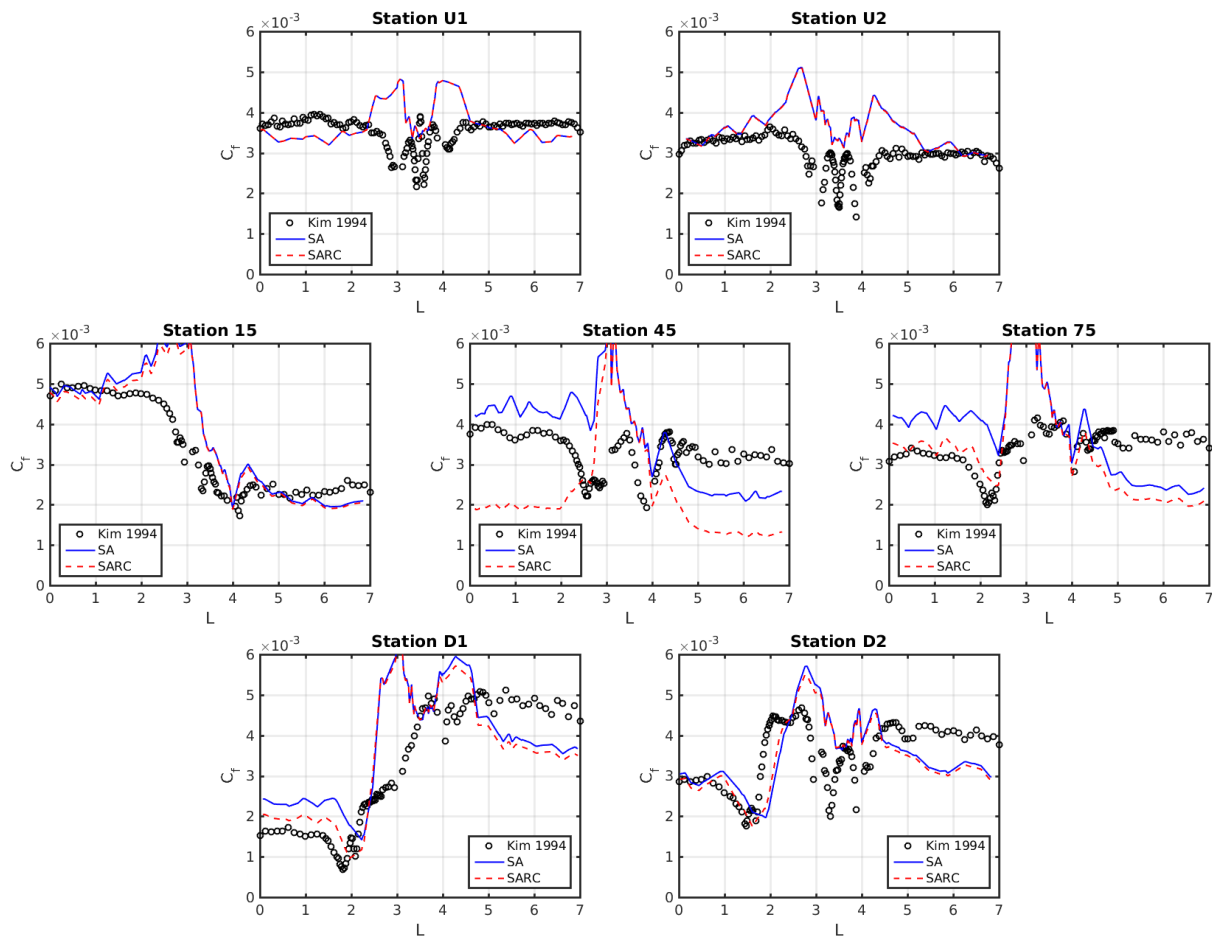
Figure 10: Wall friction coefficient data from Kim and Patel [3] (○), and the SA (——) and SARC (– – –) models at all seven experimental stations. L is defined in Figure 2.

Kim and Patel [3] also provide pressure coefficient C_p data along the inner and outer walls' centerlines, but we have not used it. Especially for debugging purposes, this could be another useful piece of information.
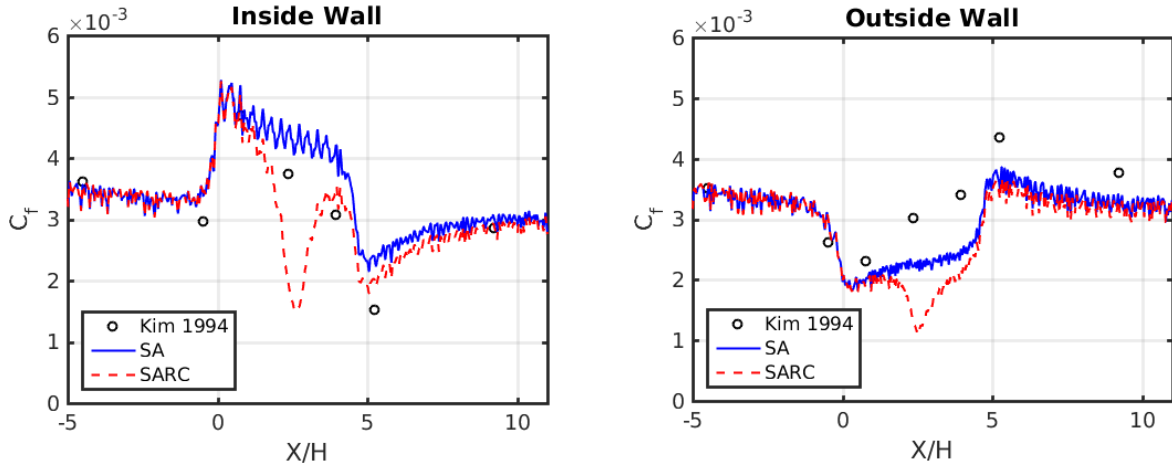
Figure 11: Wall friction coefficient data from Kim and Patel [3] (○), and the SA (——) and SARC (– – –) models from $z/H = 3$ data at all seven experimental stations.
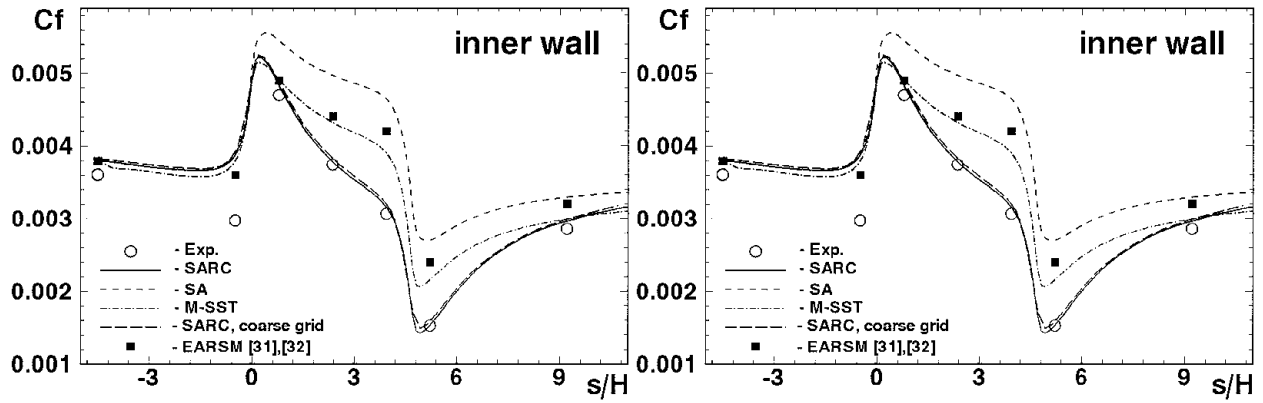
Figure 12: Centerline friction coefficient results from Shur et al. [4].

6 CONCLUSION

In conclusion, it is apparent that our implementation of the curvature-corrected SA model is, unfortunately, still incomplete. Before it can be applied to any research cases of interest, these issues will need to be addressed. Nonetheless, the process illustrates some prime difficulties of developing and validating turbulence models. In particular, obtaining an adequate estimate of boundary conditions can be daunting, especially if an experiment does not measure, say, upstream velocity profiles or other relevant parameters. Furthermore, some complex models may not have simple cases on which they can be debugged, and therefore the process of debugging may be extended due to the enhanced resource consumption required to resolve interesting model behavior. In any case, I hope to correct the current shortcomings of this SARC implementation in the near future, and hopefully we will have the capability to use SARC on the aggressive subsonic diffuser case or the high-lift wing configuration soon.

REFERENCES

[1] P. Bradshaw. Effects of streamline curvature on turbulent flow. Technical report, NATO AGARD, 1973.

[2] J. Dacles-Mariani, G. C. Zilliac, J. S. Chow, and P. Bradshaw. Numerical/experimental study of a wingtip vortex in the near field. *AIAA Journal*, 33(9):1561–1568, 1995.

[3] W. J. Kim and V. C. Patel. Origin and decay of longitudinal vortices in developing flow in a curved rectangular duct. *Journal of Fluids Engineering*, 116(1), 1994.

[4] M. L. Shur, M. K. Strelets, A. K. Travin, and P. R. Spalart. Turbulence modeling in rotating and curved channels: Assessing the Spalart-Shur correction. *AIAA Journal*, 38(5), 2000.

[5] P. R. Spalart. Young-person's guide to detached-eddy simulation grids. Technical report, NASA Langley Research Center, July 2001.

[6] P. R. Spalart and S. R. Allmaras. A one-equation turbulence model for aerodynamic flows. *AIAA 30th Aerospace Sciences Meeting*, 1992.

[7] P. R. Spalart and M. Shur. On the sensitization of turbulence models to rotation and curvature. *Aerospace Science and Technology*, (5):297–302, 1997.